UDC 539.4

Fatigue Strength and Life Prediction of a MAR-M247 Nickel-Base Superalloy Gas Turbine Blade with Multiple Carbide Inclusions

H. Lin,[a,b] H. P. Geng,[a,b,1] Y. Y. Zhang,[a,b] H. Li,[a,b] X. Y. Liu,[c] X. F. Zhou,[b] and L. Yu[a,b]

[a] School of Mechanical Engineering, Xi'an Jiaotong University, Xi'an, Shaanxi, China

[b] State Key Laboratory for Strength and Vibration of Mechanical Structures, Xi'an Jiaotong University, Xi'an, Shaanxi, China

[c] Dongfang Turbine Co. Ltd., Deyang, Sichuan, China

[1] haipenggeng@126.com

Casting of a gas turbine blade from MAR-M247 nickel-base superalloy is followed by multiple carbide precipitates as a result of solidification. The microstructure of carbide was established with scanning electron microscopy and energy spectrum analysis. A finite element model simulating the blade with a random carbide precipitate is constructed using ANSYS software, and stress-strain evaluation is performed. The blade operation conditions are realized in a vibratory-tensile combined test setup with stress measurements using strain gauges arranged on different parts of the blade. The respective von Mises equivalent stresses obtained in simulation and test measurements are found to be comparable and can be used to assess the blade fatigue life based on the available fatigue curves and Palmgren–Miner rule of damage accumulation. Simulation and experimental results are the basis for plotting the relationship between the volumetric ratio of precipitates in the blade and its fatigue life. The results obtained at room temperature can; be extrapolated to the elevated ones to provide more reliable prediction of the superalloy blade fatigue and creep-fatigue life values.

Keywords: fatigue strength, MAR-M247 nickel-base superalloy, gas turbine blade, carbide precipitates, fatigue life prediction.

Introduction. High-temperature blades in heavy-duty gas turbines are usually made of various nickel-base alloys, including MAR-M247 nickel-base superalloy. The operation conditions of gas turbine blades imply their failure via fatigue fracture mechanism [1, 2], which is accompanied by creep, mechanical structure strength, thermomechanical effect, etc. [3, 4].

In the process of nickel-base alloy casting solidification, a variety of defects is formed in the blade material [5]. This study is mainly focused on carbide defects, which exist in nickel-base superalloy, due to the reaction between elements of parent metal (M) and carbon (C) during the casting solidification and formation of carbides (MC). The total content of carbides is about one percent. These carbides are discrete and blocky precipitates of unknown shapes and sizes. They are random in the quantity, shape, and position, and unpredictable in the casting blade of the nickel-base superalloy. Therefore, carbide defects may deteriorate the strength of nickel-base superalloy, and their effect on the blade fatigue crack initiation and propagation cannot be ignored.

Nickel-base alloys are widely used as high-temperature materials. A complex airfoil surface of the gas turbine blade is produced through casting, and internal carbide defects appear simultaneously. However, the research results on the fatigue strength simulation analysis involving carbide defects are quite scarce [6]. The experimental realization of the blade operation conditions is quite problematic, since special experimental setups are required for the full-scale blade testing [7–9]. The above-mentioned carbide defects are important factors controlling the blade service performance and reliability and seriously degrading the blade superalloy mechanical structure fatigue strength and service life. Given this, the influence of carbide defects on the blade fatigue strength needs to be taken into account.

In this paper, carbide defects in MAR-M247 nickel-base superalloy are analyzed by the scanning electron microscope and the energy spectrum analysis. A finite element model simulating the blade model with a random carbide defect is elaborated via the finite element simulation software, and stress-strain calculations are performed. The blade operation conditions are experimentally realized via a vibration-tensile combined test setup with stress measurements using strain gauges applied to different parts of the blade. The respective von Mises equivalent stresses obtained via simulation and test measurements are found to be consistent and used to assess the blade fatigue life using available fatigue curves and the Palmgren–Miner rule of damage accumulation. Finally, based on the simulation and experimental results, the relationship between the volumetric ratio of defects in the blade and its fatigue life is proposed in the normal temperature state.

1. **Microstructural Characterization of Carbide Defects in a Blade**. The blade under study is the fourth stage one of the heavy-duty gas turbine. The blade is produced by casting from MAR-M247 nickel-base superalloy, which chemical composition (in wt.%) is shown in Table 1.

Table 1

The Chemical Composition of MAR-M247 Nickel-Base Superalloy

C	Cr	Mo	Al	Co	Ti	Fe	W	Hf	B	Ta	Zr	Ni
0.16	8.6	0.8	5.6	10.0	1.0	0.2	10.0	1.5	0.02	3.0	0.06	Rest

Several carbides of MC type, such as TaC, WC, TiC, HfC, etc., were found to precipitate in the above blade material during its casting process. Although their amount is small, carbides exert a significant impact on the material properties and facilitate the crack initiation and propagation, which leads to a reduced lifetime [10]. Therefore, the microstructural evaluation of the blade material and carbides is carried out in this study.

The nickel-base superalloy sample of a cubic shape ($5\times5\times10$ mm) is subjected to the scanning electron microscopy (SEM). The respective backscattered electron image obtained via JEOL JSM-6390A, (Japan) is shown in Fig. 1a. In addition, an energy dispersive X-ray spectrometer (EDS) is used to analyze the energy spectrum in the corresponding area in Fig. 1b. Finally, the surface morphology, chemical composition, and the relative content are obtained. The precipitation elements of the revealed carbides are also detected and shown in Fig. 2.

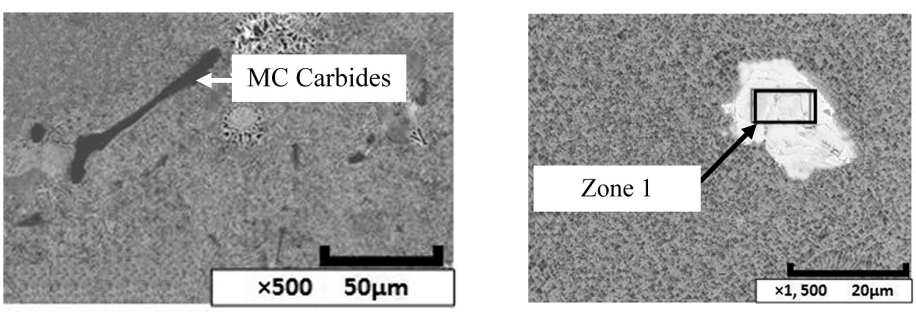

a b

Fig. 1. The metallographic analysis results via SEM: (a) MC type carbide defect; (b) compositional analysis of the identification zone.

Figure 1 depicts the metallographic photograph and shows the distribution of different phases. The distribution of MC type carbide defects can be observed in Fig. 1a, where

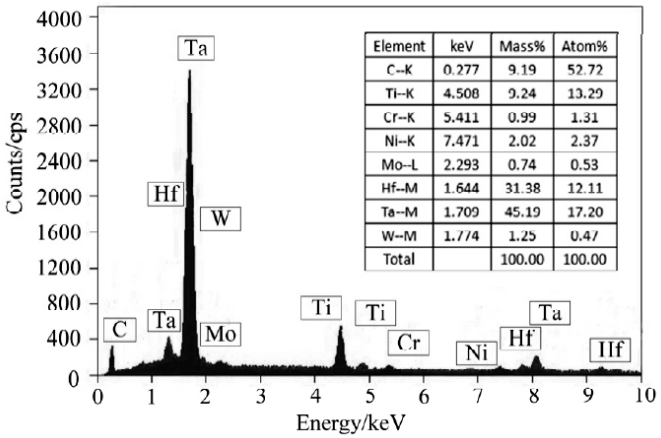

Fig. 2. Carbide defect compositional analysis by EDS.

irregular blocky carbide defects are observed in the nickel-base superalloy. Figure 1b shows the energy spectrum area in the identification zone *1*.

The carbide defect compositional analysis by EDS for the identification zone *1* is depicted in Fig. 2. The energy spectrum results strongly indicate that available carbides are based on such metals as Ta, W, Ti, and Hf, where the ratio of TaC carbide in zone *1* is the highest (over 50% of the total amount of different carbides).

2. **Finite Element Analysis**. The blocky carbide defect in the nickel-base superalloy is formed randomly during casting, so its shape is irregular, and its position inside the blade is uncertain [11]. The number of blade defects is expressed by the defect ratio in the total volume, which is a random value.

Due to the high cost of design and manufacture of heavy-duty gas turbine blades, it is essential to ensure their sufficient, but not excessive fatigue strength [12]. In this respect, the strength deterioration due to carbide defects has to be accurately estimated. The finite element method (FEM) is used in this study to simulate the defect in the blade via the finite element simulation software. The finite element model needs to reflect the shape irregularity, quantity inconsistency, and distribution randomness of carbide defects in the blade.

Within the elastic approach, the relations between displacements and strains are expressed by the following geometric deformation equations:

$$\varepsilon_x = \frac{\partial u}{\partial x}, \quad \varepsilon_y = \frac{\partial v}{\partial y}, \quad \varepsilon_z = \frac{\partial w}{\partial z}, \quad \gamma_{xy} = \frac{\partial u}{\partial y} + \frac{\partial v}{\partial x}, \quad \gamma_{yz} = \frac{\partial v}{\partial z} + \frac{\partial w}{\partial y}, \quad \gamma_{zx} = \frac{\partial u}{\partial z} + \frac{\partial w}{\partial x}, \quad (1)$$

where u, v, w are displacements in three orthogonal directions, $\varepsilon_x, \varepsilon_y, \varepsilon_z$ represent the normal strain, and $\gamma_{xy}, \gamma_{yz}, \gamma_{zx}$ represent the shear strain.

The stress-strain relation is expressed by the material physical equations:

$$\varepsilon_x = \frac{1}{E}[\sigma_x - \mu(\sigma_y + \sigma_z)], \quad \varepsilon_y = \frac{1}{E}[\sigma_y - \mu(\sigma_z + \sigma_x)], \quad \varepsilon_z = \frac{1}{E}[\sigma_z - \mu(\sigma_x + \sigma_y)],$$
$$\gamma_{xy} = \frac{2(1+\mu)}{E}\tau_{xy}, \qquad \gamma_{yz} = \frac{2(1+\mu)}{E}\tau_{yz}, \qquad \gamma_{zx} = \frac{2(1+\mu)}{E}\tau_{zx}, \quad (2)$$

where E is elastic modulus, μ is Poisson's ratio, while $\sigma_x, \sigma_y, \sigma_z$ represent normal stresses acting along the respective coordinate axes.

The relation between the stress and the external force is expressed by the force equilibrium equations:

$$\frac{\partial \sigma_x}{\partial x}+\frac{\partial \tau_{xy}}{\partial y}+\frac{\partial \tau_{zx}}{\partial z}+P_x=0, \quad \frac{\partial \sigma_y}{\partial y}+\frac{\partial \tau_{yz}}{\partial z}+\frac{\partial \tau_{xy}}{\partial x}+P_y=0, \quad \frac{\partial \sigma_z}{\partial z}+\frac{\partial \tau_{zx}}{\partial x}+\frac{\partial \tau_{yz}}{\partial y}+P_z=0, \tag{3}$$

where τ_{xy}, τ_{yz}, τ_{zx} are shear stress, while P_x, P_y, P_z represent forces acting along the respective coordinate axes.

Under the gas turbine blade operation conditions, large stresses appear in the vicinity of internal carbide defects, which act as stress raisers. Thus, the blade fatigue strength depends on the maximum local stress and strain at the stress concentration area. The calculated fatigue life corresponds to the crack initiation and propagation within a small area of stress concentration, where the stress concentration factor K_t is defined as follows:

$$K_t=\frac{\Delta\sigma_{\max}}{\Delta S}. \tag{4}$$

When estimating the blade fatigue life, the following relation linking the maximum local stress and strain ranges ($\Delta\sigma_{\max}$ and $\Delta\varepsilon_{\max}$, respectively), nominal stress range ΔS, and elastic modulus E can be used

$$\Delta\sigma_{\max}\Delta\varepsilon_{\max}=\frac{(K_t\Delta S)^2}{E}. \tag{5}$$

Hence, the blade fatigue life N can be assessed via the following equation:

$$\frac{\Delta\varepsilon_{\max}}{2}=\frac{\sigma'_f}{E}(2N)^{\mu_0}+\varepsilon'_f(2N)^{c_0}, \tag{6}$$

where σ'_f, ε'_f, μ_0, and c_0 are the material constants, which are referred to as fatigue strength factor, fatigue ductility factor, fatigue strength index, and fatigue ductility index, respectively.

A finite element model of the complete blade is constructed in ANSYS using solid 3D tetrahedron-shaped elements. Their material properties correspond to those of the nickel-base superalloy under study. Then, the respective elements corresponding to carbide defects are randomly assigned within the blade model, which number depends on the volumetric ratio of carbides and which material properties correspond to those of the particular carbide. The blade material density, elastic modulus, and Poisson's ratio are 8.2 g/mm^3, 200 GPa, and 0.3, respectively, while those of the defect element are 0.5 g/mm^3, 200 MPa, and 0.03. The yield strength of MAR-M247 was experimentally defined at 883 MPa.

The blade finite element model with boundary and loading conditions is shown in Fig. 3. The model consists of 1285,212 tetrahedron elements and 1890,929 nodes. In order to simulate the blade contact state in the operation conditions, 80,929 surface nodes of the blade shroud, joint, and flange are connected by spring elements of stiffness equal to $1\cdot10^8$, $1\cdot10^{10}$, and $1\cdot10^5$, respectively. The angular velocity of 628 rad/s is applied in the direction of the blade rotation, which corresponds to the rated speed (6000 rpm) under the actual loading conditions of the gas turbine blade.

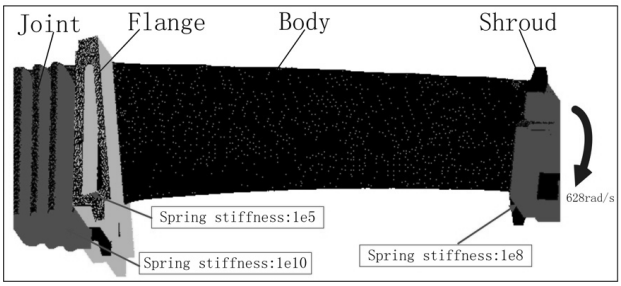

Fig. 3. Turbine blade finite element model.

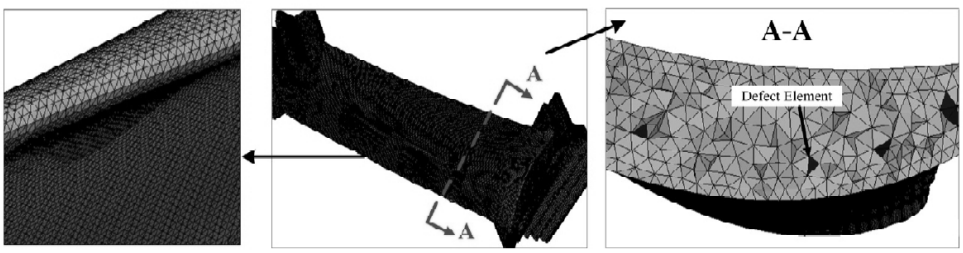

Fig. 4. The finite element model including the defect element.

The defect tetrahedron-shaped element in the tangent section of the blade is shown in Fig. 4. The finite element model can not only simulate the carbide defect size, but also reflect its irregularity and randomness in the cast nickel-base superalloy blade.

Because of the complex shape and variable thickness of the blade body, casting-induced defects are likely to form at its airfoil and produce stress raisers, which make it more prone to accelerated fatigue failure than other turbine parts. Therefore, carbide defects are assumed to exist in the blade body.

Firstly, the volumetric ratio of 0.02% is preset for carbide defects in the FEM calculation via ANSYS software. Figure 5 shows the calculation results for the blade equivalent stress distribution in the pressure and suction surfaces. The positive stress values are shown to grow from the blade bottom to its top, where the maximum value of 637 MPa is reached.

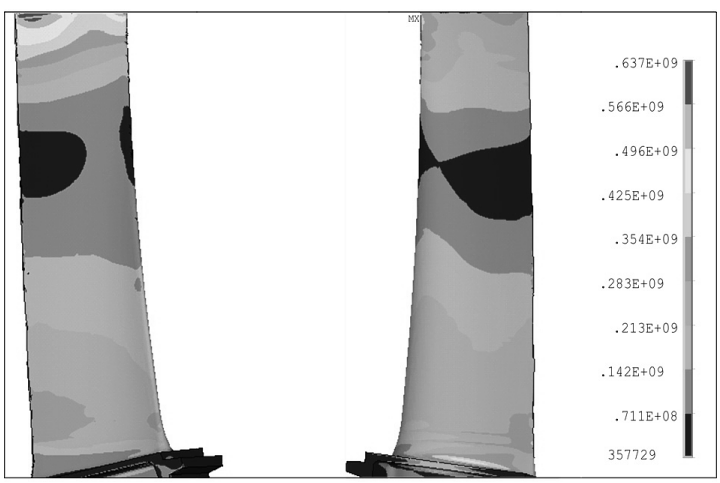

Fig. 5. Von Mises stress distribution nephograms (in Pa).

Based on the above stress analysis results, the blade fatigue life can be estimated using the available fatigue curve (S–N curve). As shown in Fig. 6, blade fatigue life distribution nephograms of the pressure and suction surfaces represent the number of cycles to failure (fatigue life) of different blade parts with assumed inherent carbide defects. The shortest fatigue life in the blade body is assessed at $1.99 \cdot 10^6$ cycles and corresponds to the most stressed top of the blade, while that of the blade middle part is $1 \cdot 10^7$ cycles, which implies that its stress level is nearly equal to the fatigue life limit.

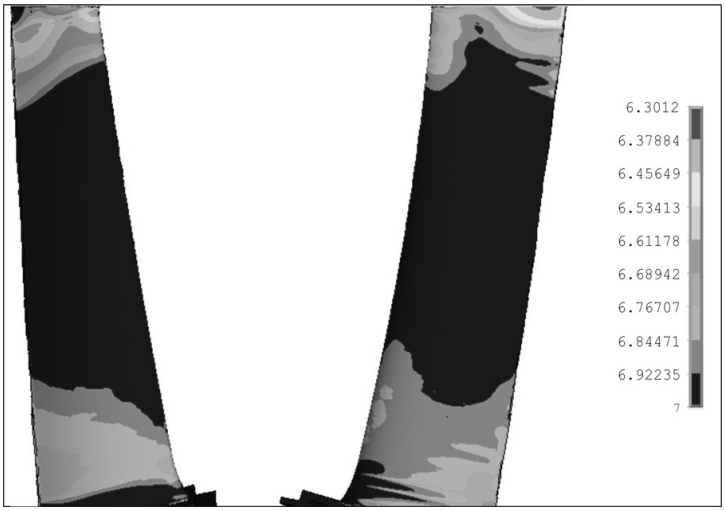

Fig. 6. Fatigue life distribution nephograms (in 10^n).

3. **Blade Strength Test and Dynamic Stress Measurements**. For the heavy-duty gas turbine blade, it is quite problematic to simulate its true operation conditions by fatigue tests under laboratory conditions [13]. Therefore, as shown in Fig. 7, a special experimental setup, which provided mechanical fatigue conditions simulating the blade operation one, was elaborated in this study. The experimental setup comprises (i) adjusting devices for the fixation of the blade shroud, joint, and flange; (ii) a high-frequency micro-amplitude vibration bench for simulating the blade contact state in the operation conditions; (iii) a tensile loading device, which is applied to the blade shroud to simulate the centrifugal force action under the rated speed of 6000 rpm.

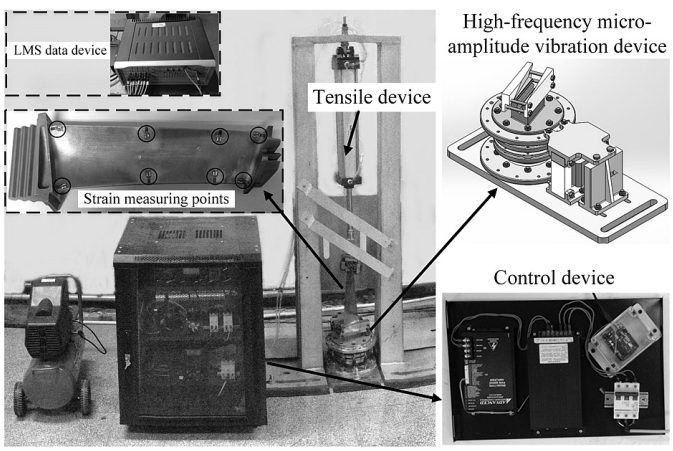

Fig. 7. Fatigue experimental setup for the blade.

The blade fatigue life is mainly determined by scattered defects located within a large damage area. In this experiment, the top, middle and bottom parts of the blade body were selected as measuring points, with placement of strain sensors. There were two measuring points in the bottom, two measuring points in the middle, and four measuring points in the top. The LMS data device was used to acquire the dynamic stress data of the blade in the real time scale.

The experimental data obtained were processed with the elimination of interference signals [14]. Eventually, the experimental stress values in measuring points were obtained at the data sampling frequency of 20,480 Hz. Then, the experimental data obtained were used to plot the stress–time history in the measuring points, which are depicted in Fig. 8.

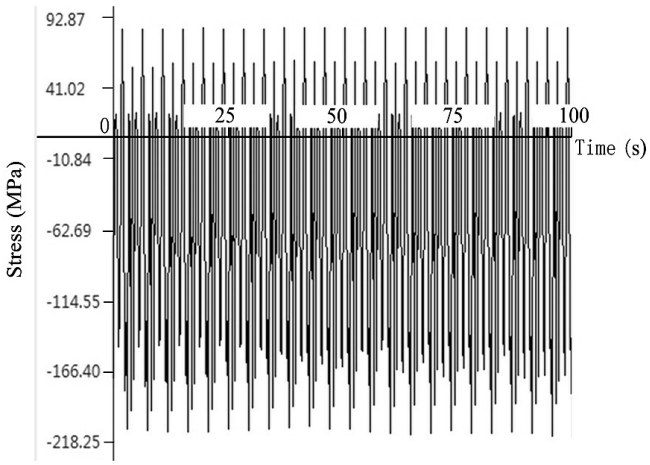

Fig. 8. Experimental stress–time history.

According to the experimental results, the maximum stress values in the top, middle, and bottom of the blade body were equal to 657, 382, and 545 MPa, respectively, which did not exceed the blade yield strength of 883 MPa. As shown in Table 2, the maximum stress area was observed in the top of the blade body, and the minimum one in its middle.

Table 2

Experimental Maximum Stress and Fatigue Life Values

Measuring point	Top				Middle		Bottom	
	1	2	3	4	5	6	7	8
Maximum stress value (MPa)	657	636	550	503	337	382	519	545
Fatigue life ($\times 10^6$, cycles)	1.0	1.55	1.78	4.90	7.0	7.0	6.46	5.89

The estimation of fatigue life of a blade subjected to cyclic loading with a variable stress amplitude is based on the damage accumulation principle. When the blade is subjected to the stress below the fatigue strength limit, each stress cycle produces a certain amount of damage. The damage is accumulated, and the failure occurs when the damage achieves its critical value.

According to the Palmgren–Miner linear fatigue cumulative damage rule [15], the material fatigue damage at each stress level is accumulated independently of previous or next levels, and the total damage can be superimposed linearly [16]. The critical failure value D is assumed to be

$$D = \sum_{i=1}^{l} \frac{n_i}{N_i} = 1. \tag{7}$$

For the experimental measured stress amplitude of σ_l, the damage caused by n cycles in the test loading sequence can be expressed as follows:

$$D_l = \sum \frac{n\sigma_l^m}{C}, \tag{8}$$

where C and m are the material constants controlling the regression line of the blade *S–N* curve.

Suppose that fatigue failure is achieved when the superposition of the number of cycles at the fatigue limit value σ_a adds up to $N_a = 10^7$ cycles.

According to Eq. (7), the number of cycles corresponding to the particular measured stress amplitude can be calculated by the following equation:

$$\frac{N_a\sigma_a^m}{C} = L\sum \frac{n\sigma_l^m}{C}, \tag{9}$$

where L is a constant.

The fatigue life values of each measuring point calculated from the experimental data are listed in Table 2. The minimum fatigue life values in the top, middle, and bottom of the blade body were assessed as $1.17 \cdot 10^6$, 10^7, and $5.89 \cdot 10^6$ cycles, respectively. Thus, the life of the total blade is limited by the shortest fatigue life of $1.17 \cdot 10^6$ cycles of its top part.

4. **Results and Discussion**. The comparison of experimental data and simulation results is illustrated by Fig. 9. The experimental curves comprise the experimental data of eight measured points, while the simulation curves show the simulation distribution of stress and fatigue life values.

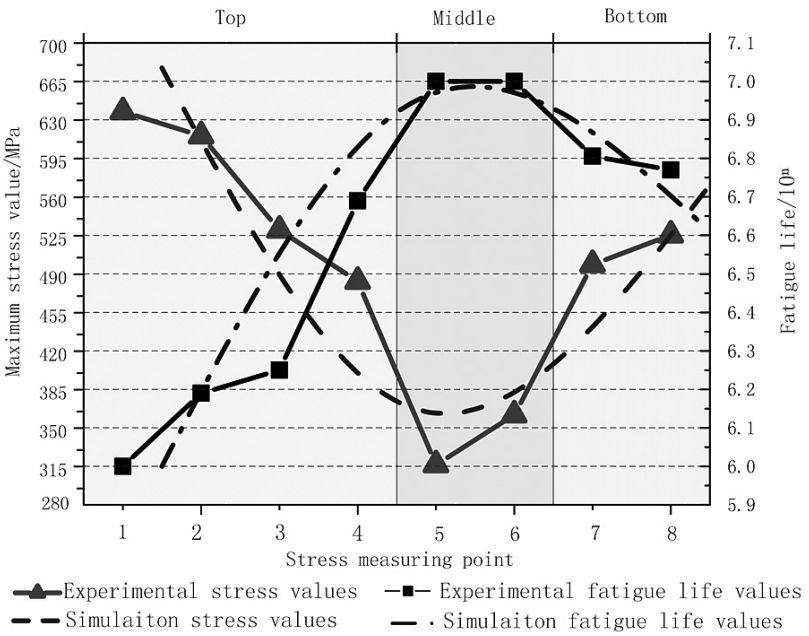

Fig. 9. Comparison of experiment and simulation results.

The comparative analysis of experimental data and simulation results in Fig. 9 reveals their close fit for both stress and fatigue life values, including the general evolution trends throughout the blade body. This implies a feasibility of the applied FEM approach. Insofar as the simulation values are slightly larger than the experiment ones, this implies the blade strength evaluation in this study is conservative, and the simulation results on the blade fatigue life assessment are reliable.

The applied FEM approach made it possible to construct blade models with various defect volumetric ratio, namely: 0.02, 0.05, 0.08, 0.1, 0.015, 0.2, and 0.5%. For each of these cases, the finite element simulation yielded the maximum stress and minimum fatigue life values. The respective curves of the maximum stress and minimum fatigue life values corresponding to different defect ratios ranging from 0.02 to 0.5% are shown in Fig. 10.

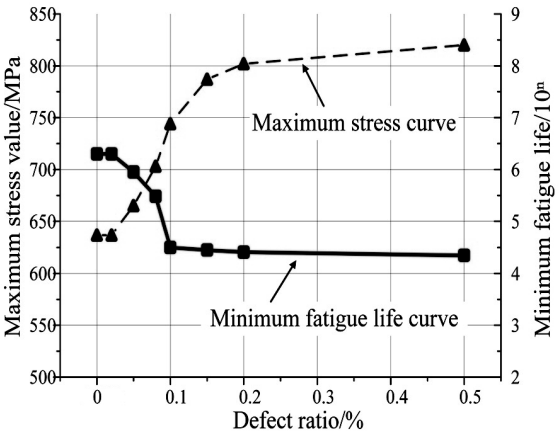

Fig. 10. Curves for different defect ratios.

From the calculation results, it can be seen that different defect ratios affect the stress distribution over the blade body. The maximum stress value increases from 637 to 820 MPa, which is yet smaller than the yield strength of 883 MPa. When the defect ratio drops below 0.01%, the maximum stress value is equal to that in a defect-free blade. Thus, calculation results properly reflect the mechanical conditions of the actual blade defects.

With an increase in the defect ratio, the minimum fatigue life is reduced from $1.99 \cdot 10^6$ to $2.24 \cdot 10^4$ cycles. When the defect ratio is below 0.01%, the shortest fatigue life is equivalent to the fatigue life level of a defect-free blade. The results obtained show that the proposed finite element model with different defect ratios is instrumental in the assessment of the maximum stress and minimum fatigue life values.

From the above Fig. 10, the variation trend of predicted maximum stress and fatigue life cycle number values can be observed, and the shape type of the trend can be approximatively an L-shaped. The points of maximum stress and fatigue life cycle number values are shown in Figs. 11 and 12. Through the distribution of value points estimated, values can be fitted as different function types, such as sine function, Gauss function, logistic function, etc.

The comparative analysis of different function fitting results reveals the fitting of the logistic function model is the closest for both stress and fatigue life values.

The fitting function model of the predicted maximum stress value S is expressed by the following equation:

$$S = A_2 + (A_1 - A_2) / [1 + (Q/q_1)^{p_1}], \tag{10}$$

where Q is the percent of defect ratios, and values of coefficients A_1, A_2, q_1, and p_1 are shown in Fig. 11. The fitting degree (adj. R-square) is 0.99659.

The fitting function model of the fatigue life cycle number N is expressed by the following equation:

$$N = A_4 + (A_3 - A_4)/[1 + (Q/q_2)^{p_2}], \tag{11}$$

where values of coefficients A_3, A_4, q_2, and p_2 are shown in Fig. 12. The fitting degree (adj. R-square) is 0.99568.

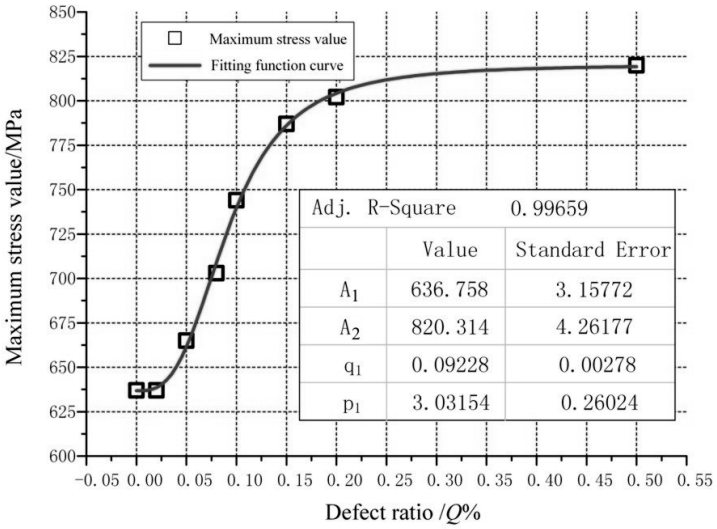

Fig. 11. Fitting function curve of maximum stress.

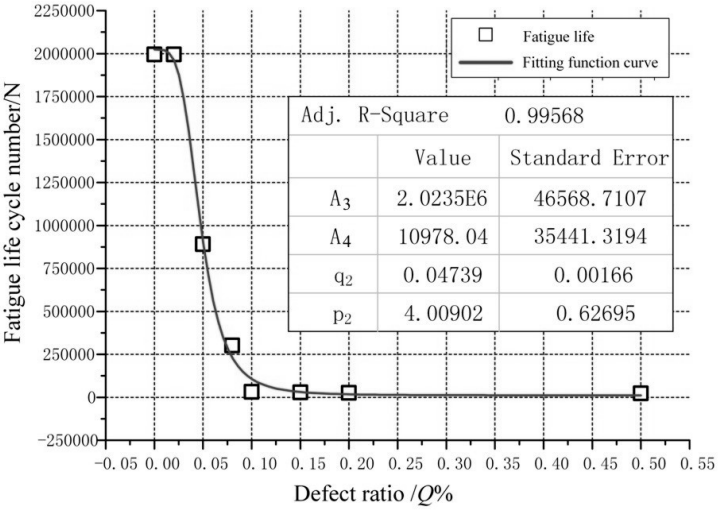

Fig. 12. Fitting function curve of fatigue life cycle number.

Figures 11 and 12 show that the fitting degree of function models is very high. Therefore, the predicted regularity of maximum stress and fatigue life cycle number can be defined by Eqs. (10) and (11). And the maximum stress value S and the fatigue life cycle

number N can be predicted by the defect ratio value Q (%). So the numerical prediction method is given and provides an effective support to study on the blade maximum stress and fatigue life under different defect ratios. It is significant for the fatigue strength prediction of the gas turbine blade with a random defect ratio.

This first attempt covered the normal temperature state, while gas turbine blades operate at high temperatures, where fatigue and creep interaction is observed, as well as evolution of MC-type carbides into $M_{23}C_6$ ones. In view of high fatigue resistance of MAR-M247 superalloy at temperatures of 650, 700, and 900℃ reported in [17], the proposed approach can be extended to the high-temperature range of the blade applications. The respective follow-up studies are envisioned by the authors.

Conclusions

1. MAR-M247 nickel-base superalloy blade material was analyzed by the scanning electron microscope, and the MC-type carbide defects, such as TaC, WC, TiC, and HfC, were observed. Then the compositional analysis of carbide defects by the energy spectrum analysis was performed, which depicted that TaC carbides amounted to 50% of the total volume of revealed carbides.

2. Based on the above results, the finite element model for the simulation of the turbine blade with randomly located carbide defects was constructed via the ANSYS software, and stress-strain calculations were performed. Meanwhile, the blade operation conditions were experimentally realized via a vibration-tensile combined experimental setup with stress measurements using strain gauges applied to different parts of the blade.

3. The respective von Mises equivalent stresses obtained via simulation and test measurements were found to be consistent and used to assess the blade fatigue life using available fatigue curves and the Palmgren–Miner rule of damage accumulation.

4. Finally, based on the simulation and experimental results, the relationship between the volumetric ratio of defects in the blade and its fatigue life was obtained. Further steps on the model refinement and its extension to high temperatures are discussed, which are assumed to have practical engineering significance.

Acknowledgments. This work was supported by National Program on Key Basic Research Projects of China (No. 2013CB03570401), Program on Industry Science and Technology Development Foundation of SAIC Motor (No. 20171039) and Core Components of High-end Energy Power Equipment in Shaanxi Province and Project of Running Diagnostic Public Platform (No. [2017] 377).

1. T. J. Carter, “Common failures in gas turbine blades,” *Eng. Fail. Anal.*, **12**, No. 2, 237–247 (2005).
2. E. Poursaeidi, M. Aieneravaie, M. R. Mohammadi, “Failure analysis of a second stage blade in a gas turbine engine,” *Eng. Fail. Anal.*, **15**, No. 8, 1111–1129 (2008).
3. Z. Mazur, A. Luna-Ramirez, J. A. Juárez-Islas, and A. Campos-Amezcua, “Failure analysis of a gas turbine blade made of Inconel 738LC alloy,” *Eng. Fail. Anal.*, **12**, No. 3, 474–486 (2005).
4. W. N. Yoon, M. S. Kang, N. K. Jung, et al., “Failure analysis of the defect-induced blade damage of a compressor in the gas turbine of a cogeneration plant,” *Int. J. Precis. Eng. Man.*, **13**, No. 5, 717–722 (2012).
5. X. B. Zhao, L. Liu, C. B. Yang, et al., “Advance in research of casting defects of directionally solidified nickel-based single superalloys,” *J. Mater. Eng.*, No. 1, 93–98 (2012).
6. Y. H. Xie and Q. J. Meng, “Numerical model for steam turbine blade fatigue life,” *J. Xi’an Jiaotong Univ.*, **36**, No. 9, 912–915 (2002).

7. R. J. Sun and X. J. Yan, "New characteristics of fatigue-creep tests on serration of turbine blades," *J. Aerospace Power*, **22**, No. 3, 419–424 (2007).
8. X. J. Yan and J. X. Nie, "New experimental approach in determining creep/fatigue life of directionally solidified alloy turbine blade," *J. Aerospace Power*, **20**, No. 6, 925–931 (2005).
9. H. Lin, H. P. Geng, and X. F. Zhou, "Stress characteristic study of heavy-duty gas turbine blade under centrifugal load," *J. Mech. Eng.*, **53**, No. 22, 212–218 (2017).
10. H. S. Whitesell and R. A. Overfelt, "Influence of solidification variables on the microstructure, macrosegregation, and porosity of directionally solidified MAR-M247," *Mater. Sci. Eng. A*, **318**, Nos. 1–2, 264–276 (2001).
11. L. R. Liu, T. Jin, N. R. Zhao, et al., "Effect of carbon additions on the microstructure in a Ni-base single crystal superalloy," *Mater. Lett.*, **58**, Nos. 17–18, 2290–2294 (2004).
12. X. Yan, X. Chen, R. Sun, et al., "Investigation on material's fatigue property variation among different regions of directional solidification turbine blades – Part I: Fatigue tests on full-scale blades," *J. Eng. Gas Turbines Power*, **136**, No. 10, 102502 (2014), doi: 10.1115/1.4027928.
13. H. Lin, H. Geng, H. Li, et al., "Effects of thermal and mechanical combined load on blade stress and fatigue life characteristic," in: Proc. of the IEEE Int. Conf. on Mechatronics and Automation (August 6–9, 2017, Takamatsu, Japan), IEEE (2017), pp. 1348–1353.
14. I. Rychlik, "A new definition of the rainflow cycle counting," *Int. J. Fatigue*, **9**, No. 2, 119–121 (2014).
15. S. M. Muzakkir, K. P. Lijesh, and H. Hirani, "Tribological failure analysis of a heavily-loaded slow speed hybrid journal bearing," *Eng. Fail. Anal.*, **40**, 97–113 (2014).
16. H. Lin, H. Geng, X. Zhou, et al., "High cycle fatigue analysis of third stage blade based on shroud gap effect," in: Proc. of the IEEE Int. Conf. on Mechatronics and Automation (August 7–10, 2016, Harbin, China), IEEE (2016), doi: 10.1109/ICMA.2016.7558834.
17. M. Šmid, L. Kunz, P. Hutař, and K. Hrbáček, "High cycle fatigue of nickel-based superalloy MAR-M 247 at high temperatures," *Procedia Engineer.*, **74**, 329–332 (2014).

Received 15. 03. 2018